Photoluminescence from Single-Walled MoS₂ Nanotubes Coaxially Grown on Boron Nitride Nanotubes

Ming Liu[1], Kaoru Hisama[1], Yongjia Zheng[1], Mina Maruyama[2], Seungju Seo[1], Anton Anisimov[3], Taiki Inoue[1,4], Esko I. Kauppinen[5], Susumu Okada[2], Shohei Chiashi[1], Rong Xiang[1], and Shigeo Maruyama[1]*

[1] *Department of Mechanical Engineering, The University of Tokyo, Tokyo 113-8656, Japan*

[2] *Graduate School of Pure and Applied Sciences, University of Tsukuba, Tsukuba 305-8571, Japan*

[3] *Canatu Ltd., Helsinki FI‐00390, Finland*

[4] *Department of Applied Physics, Graduate School of Engineering, Osaka University, Osaka 565-0871, Japan*

[5] *Department of Applied Physics, Aalto University School of Science, Espoo 15100, FI-00076 Aalto, Finland*

*email: maruyama@photon.t.u-tokyo.ac.jp

Abstract

Single-walled and multi-walled molybdenum disulfide (MoS_2) nanotubes have been coaxially synthesized on small diameter boron nitride nanotubes (BNNTs) that are obtained from removing single-walled carbon nanotubes (SWCNTs) in heteronanotubes of SWCNTs coated by BNNTs, and have been systematically investigated by optical spectroscopy. The photoluminescence (PL) from single-walled MoS_2 nanotubes supported by core BNNTs is observed in this work, which evidences the direct bandgap structure of single-walled MoS_2 nanotubes with a diameter around 6 - 7 nm. The observation is consistent with our DFT results that the single-walled MoS_2 nanotube changes from an indirect-gap to a direct-gap semiconductor when the diameter of a nanotube is more than around 5.2 nm. On the other hand, when there are SWCNTs inside the heteronanotubes of BNNTs and MoS_2 nanotubes, the PL signal is considerably quenched. The charge transfer and energy transfer between SWCNTs and single-walled MoS_2 nanotubes were examined through characterizations by PL, X-ray photoelectron spectroscopy (XPS), and Raman spectroscopy. Unlike single-walled MoS_2 nanotubes, multi-walled MoS_2 nanotubes have an indirect bandgap, and the PL from multi-walled MoS_2 nanotubes is significantly quenched. Single-walled and multi-walled MoS_2 nanotubes exhibit different Raman features in both resonant and non-resonant Raman spectra. The method of assembling heteronanotubes using BNNTs as templates provides an efficient approach for exploring the electronic and optical properties of other transition metal dichalcogenide nanotubes.

Keywords: one-dimensional heterostructure, molybdenum disulfide nanotubes, single-walled carbon nanotubes, photoluminescence, Raman spectroscopy, bandgap

Van der Waals heterostructure of two-dimensional (2D) layered materials[1] have attracted much attention in material research since the first experimental isolation of single-layer graphene.[2-7] The intriguing properties in heterostructures with diverse layerings of metal, semiconductors or insulators have raised numerous designs of electronic devices as well as optoelectronic devices. Atomically thin transition-metal dichalcogenide (TMD) such as MoS_2 holds great promise for electrical, optical, and mechanical devices, as well as interesting physical phenomena.[8] Meanwhile, wrapping 2D TMD materials into 1D nanotubes has brought interests in creating chiral tubular structure and radial heterojunctions with diverse functionalities.[9] Recently, we have demonstrated one-dimensional (1D) van der Waals heterostructures templated on single-walled carbon nanotubes (SWCNTs).[10] 1D van der Waals materials will join the innovation of electronic and optoelectronic devices with 2D layered materials.

Fullerene-like and nanotube structures of MoS_2 have been firstly produced by a gas-phase reaction firstly in 1995.[11] A combined theoretical and experimental work has indicated that multi-walled MoS_2 nanotubes (MoS_2NTs) are more stable than single-walled MoS_2NTs, while single-walled MoS_2NT with diameter more than about 6 nm is more stable than nanoribbon shape.[12] The conventional methods for growing MoS_2NTs can be divided into sulfurization[11] and chemical transport reaction.[13] The MoS_2NTs produced by these methods have the diameter between tens of nanometers to several micrometers with multiple walls.[14] Subnanometer-diameter single-wall MoS_2 nanotubes have been reported before,[15] yet the electronic and optical properties of MoS_2 nanotubes were not studied in this work. The bulk form of MoS_2 is an indirect bandgap semiconductor with an energy gap of ~1.2 eV[16] and when the thickness reduces to a single layer, the band gap of MoS_2 changes from indirect to direct.[17] In addition, recent studies have showed the strong photoluminescence in monolayer MoS_2 that can be attributed to the direct-gap electronic structure.[18-20] The band structure of single-walled and multi-walled MoS_2NTs are still not well investigated experimentally, though modulated calculations have predicted that MoS_2NTs have indirect bandgaps except those with zigzag chiral indices.[21-23] Here, although the zigzag MoS_2NTs are calculated as direct-gap semiconductors, the band edge states are predicted to come from different subbands and PL is not expected.[24]

Using a tubular template to confine the formation of inorganic nanotubes has been proposed to stabilize few-walled inorganic nanotubes, which is a critical step toward understanding their

optical properties and implementing into electronic and optoelectronic devices. Carbon nanotubes (CNTs) have been used as a template to assemble specific materials[25, 26] and as filling vessels for metals[27, 28] for forming core-shell nanotubes. Charge transfer from a CNT core to a MoS_2 sheath has been verified by X-ray photoelectron spectroscopy in a composite MoS_2/CNT material.[29] The ultrafast optoelectronic processes in 1D heterostructures have been investigated lately.[30] Core-shell carbon@MoS_2 nanotube sponges have been utilized as electrodes in a high-performance battery.[31] However, single-walled MoS_2NTs are rarely observed in the previous core-shell inorganic nanotube studies. Besides, CNTs are optically active materials with high response signal of Raman spectra[32] and photoluminescence spectra,[33] which makes the investigation of optical properties of the TMD shell outside a CNT infeasible. Hence, boron nitride nanotube (BNNT) is a promising substitute for serving as a template to research the optical properties of the shell materials since the band gap of BNNTs is ~5.5 eV which is large enough to be transparent within a wide range of wavelengths and quasi-independent from the chirality.[34]

In this paper, we present a systematic study of the optical properties and electronic structure of MoS_2NTs including single-walled and multi-walled types. We have developed a facile chemical vapor deposition (CVD) method for synthesizing the core-shell BNNT and MoS_2NTs which starts from removing the SWCNT in the heteronanotube of SWCNT coated by BNNT (SWCNT@BNNT). The hetero structure based on BNNTs is a promising platform for studying the optical properties of MoS_2 layers or other TMD layers. The properties of various heteronanotubes were examined by using three complementary spectroscopic techniques: optical absorption, Raman spectroscopy, and photoluminescence (PL), with additional characterizations provided by transmission electron microscopy (TEM) and DFT calculations using the STATE (Simulation Tool for Atom Technology) package. The PL signal from single-walled MoS_2NTs indicates the direct band gap structure of the material, which is consistent with our DFT results. With increasing the wall number of MoS_2NTs, the PL signal decreased significantly which allows us to trace the direct and indirect bandgaps structure of the MoS_2NTs. The charge and energy transfer between SWCNTs and MoS_2NTs in the 1D hetero structure were observed in this work.

Results and Discussion

    Synthesis and structure analysis of BNNT@MoS$_2$NT heteronanotubes. In this work, we presented a template-assisted approach involving a sequence of facile CVD processes using SWCNTs as a template to produce different types of heteronanotubes of BNNTs with MoS$_2$NTs. The SWCNT film prepared by areosal CVD was used as a template and transferred onto a ceramic washer with the size of 4 mm inner diameter and 6 mm outer diameter. Firstly, the suspended SWCNT film on the washer was used as a template and ammonia borane was employed as the precursor to form a coaxial tube structure of SWCNT@BNNT. Then the SWCNT@BNNT film was annealed at 610℃ in the oxygen atmosphere with the pressure of 85 kPa for 12 hours to remove the SWCNTs in the film. The optical image of the as-synthesized BNNT film after the annealing process is shown in Figure 1a. The absorption spectra of SWCNT, SWCNT@BNNT, and BNNT films are shown in Figure S1a. After the removal of SWCNTs in the SWCNT@BNNT film, the obtained BNNT film is relatively transparent within the visible range of wavelengths, with one absorption peak near 205 nm. The Raman peak at ~1370 cm^{-1} was detected in Figure S1b, which is corresponding to the E$_{2g}$ in-plane vibrational mode of the h-BN networks. The Raman peak at 1555.5 cm^{-1} in Figure S1b is the vibrational mode of oxygen. In the Fourier
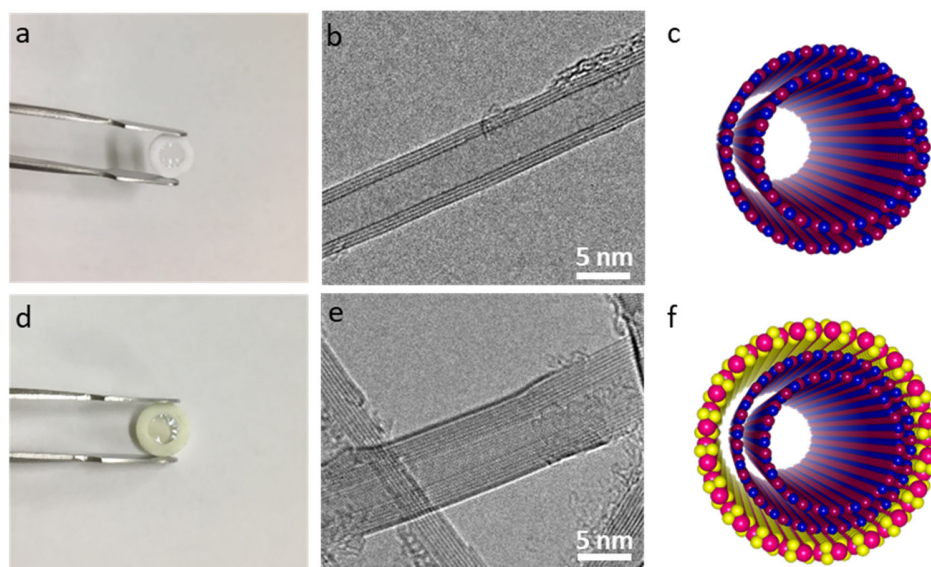

Figure 1. (a) Optical image of the suspended BNNT film on a ceramic washer. (b) Representative high-resolution TEM image of a multi-walled BNNT. (c) Atomic model of a multi-walled BNNT. (d) Optical image of the suspended BNNT@MoS$_2$NT nanotubes film on a ceramic washer. (e) Representative high-resolution TEM image of a BNNT@MoS$_2$NT. (f) Atomic model of a BNNT@MoS$_2$NT.

transformed infrared (FT-IR) spectrum (Figure S1c), the absorption band at ~1369.5 cm^{-1} is attributed to the in-plane stretching mode of the h-BN that vibrates along the longitudinal or tube axis of a BNNT. Besides, the peak at ~1520 cm^{-1} corresponds to the stretching of the h-BN along the tangential directions of a BNNT. This stretching mode smears out for h-BN bulks or thin films, and only shows up when the tube curvature induces an anisotropic strain on the h-BN which indicates the high crystallinity of BNNTs.[35] The representative high-resolution TEM image and the atomic model of a high quality BNNT are presented in Figure 1, b and c. The as-synthesized BNNT film on a ceramic was a template for the MoS$_2$ CVD process to form the heteronanotube of BNNT with single-walled MoS$_2$NT (BNNT@MoS$_2$NT). The MoS$_2$ CVD was conducted at 530 °C with the sulfur (5 g) and MoO$_3$ powders (35 mg) as precursors. The typical growing time of MoS$_2$ at 530 °C is 10 min and the optical image of BNNT@MoS$_2$NT film is shown in Figure 1d. In Figure 1e, the representative TEM image of the BNNT@MoS$_2$NT, the diameter of the outer layer single-walled MoS$_2$NT is around 6.8 nm. For the multi-walled BNNT inside MoS$_2$NT, it has the inner diameter around 2.1 nm and the outer diameter around 6.1 nm. The van der Waals distance between the BNNT and the MoS$_2$ layer is approximately 0.5 nm in the BNNT@MoS$_2$NT. The atomic model of a BNNT@MoS$_2$NT heteronanotube is presented in Figure 1f. In the BNNT@MoS$_2$NT heteronanotube, there is no chemical bonding between BN layer and MoS$_2$ layer.

Photoluminescence from single-walled MoS$_2$NTs **and the charge and energy transfer between SWCNT and** MoS$_2$NT**.** Figure 2a shows the atomic model of two types of heteronanotubes that we used to compare, SWCNT@BNNT@MoS$_2$NT and BNNT@MoS$_2$NT heteronanotubes. The PL, Raman, and absorption spectra of the two heteronanotubes are compared in Figure 2b, 2c, and 2d, respectively. The SWCNT@BNNT@MoS$_2$NT heteronanotube was synthesized by the serial CVD method described in our previous work.[10] The representative TEM image of the SWCNT@BNNT@MoS$_2$NT heteronanotube is shown in Figure S2. Optical measurements by PL, Raman, and absorption spectroscopy were performed on the free-standing SWCNT@BNNT@MoS$_2$NT and BNNT@MoS$_2$NT heteronanotube films on ceramic washers. All optical measurements were conducted under ambient conditions at room temperature. The excitation wavelength of Raman and PL spectroscopy was 532 nm (2.33 eV) with a spot diameter of ~2 μm focused on the sample. A low laser power of ~70 μW (out of the microscope) was applied to avoid heating and PL saturation.[36] Appreciable PL was observed from single-walled MoS$_2$NTs coaxially grown on BNNTs, the BNNT@MoS$_2$NT samples. The measured PL intensities for a

BNNT@MoS$_2$NT and a SWCNT@BNNT@MoS$_2$NT sample under the identical excitation at 2.33 eV are significantly different (Figure 2b). The PL intensity of SWCNT@BNNT@MoS$_2$NT sample is eight times less than the PL signal from the BNNT@MoS$_2$NT sample. However, the shape of the normalized PL spectra for both samples are nearly identical. The PL spectrum of BNNT@MoS$_2$NT consists a single feature centered at 1.85 eV. In contrast, the center of the PL peak for SWCNT@BNNT@MoS$_2$NT is at 1.87 eV, slightly blue shifted. The sharp peaks in both PL spectra are from the Raman signal of the MoS$_2$ and SWCNT in the film.
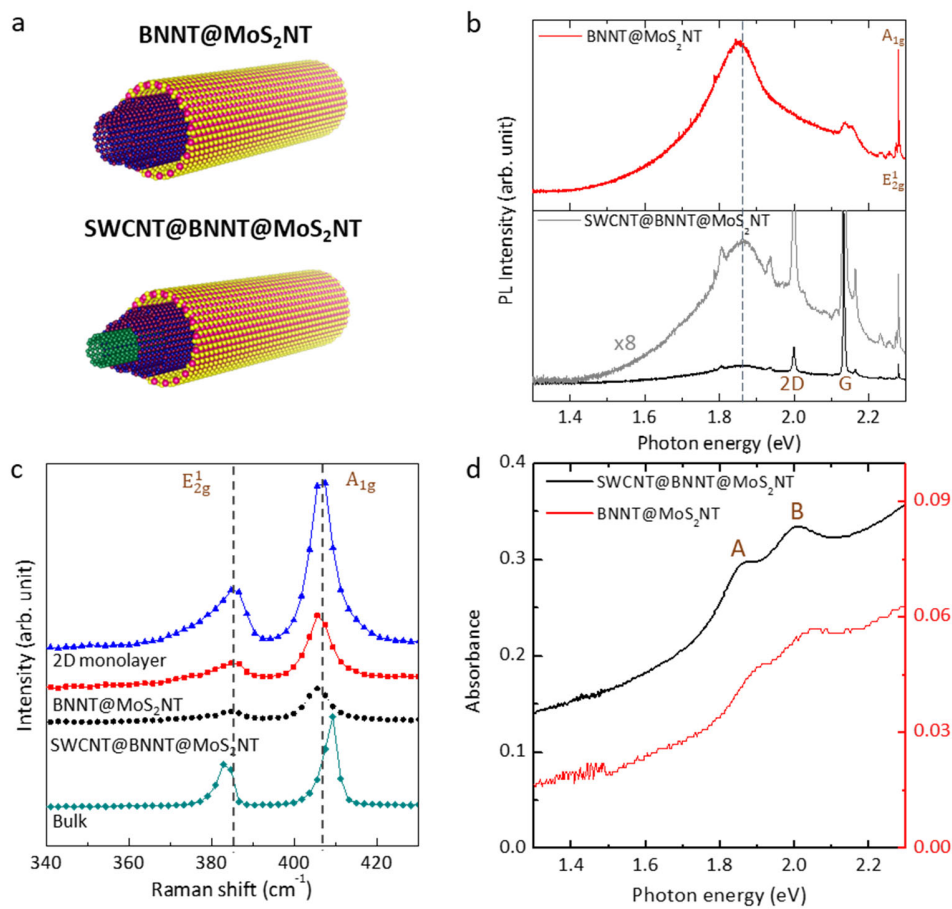

Figure 2. (a) The atomic model of a BNNT@MoS$_2$NT heteronanotube and a SWCNT@BNNT@MoS$_2$NT heteronanotube. (b) The PL spectra of BNNT@MoS$_2$NT and SWCNT@BNNT@MoS$_2$NT, respectively. The black dot line is the eight times enlarged PL spectrum of SWCNT@BNNT@MoS$_2$NT. (c) Representative Raman spectra of 2D monolayer MoS$_2$, BNNT@MoS$_2$NT, SWCNT@BNNT@MoS$_2$NT, and bulk MoS$_2$. (d) Representative absorption spectra of free-standing SWCNT@BNNT@MoS$_2$NT and BNNT@MoS$_2$NT films.

To understand the origin of the extraordinary PL property from single-walled MoS_2NTs, we compared the PL spectra with the absorption spectra of these samples (Figure 2d). In the range of 1.3–2.3 eV, there are two main absorption peaks that are contributed to the direct-gap transitions between the maxima of split valence bands ($v1$ and $v2$) and the minimum of the conduction band ($c1$) which are all located at the K point of the Brillouin zone.[37-39] The PL peak of $BNNT@MoS_2NT$ at 1.85 eV matches the lower absorption resonance (conventionally called A exciton) in the absorption spectrum. Therefore, we assigned the PL of $BNNT@MoS_2NT$ to direct-gap luminescence. The upper absorption resonance (B exciton) is observed in $SWCNT@BNNT@MoS_2NT$ and $BNNT@MoS_2NT$, however the PL emission from B exciton is not observed in our experiment. In Figure 2d, the absorption of MoS_2 for $BNNT@MoS_2NT$ sample and $SWCNT@BNNT@MoS_2NT$ sample is quite different. There are several factors that could explain the stronger A and B peaks in $SWCNT@BNNT@MoS_2NT$ sample: (1) $SWCNT@BNNT@MoS_2NT$ sample still contains SWCNT, and as shown in Figure S3(a) SWCNT has a broad absorption around A and B peak. This would add up the absorption intensity of A and B peak in $SWCNT@BNNT@MoS_2NT$ sample. (2) In our experiment, the BNNT film was obtained by O_2 annealing SWCNT@BNNT sample. Then the SWCNTs not fully coated by BN might be burned during the annealing process which could result in the lower density of nanotubes in BNNT film. Thus, the overall amount of MoS_2 coating on SWCNT@BNNT and BNNT films is a bit different. (3) In $SWCNT@BNNT@MoS_2NT$ heteronanotubes, SWCNT and MoS_2NT might form a staggered-gap alignment and intertube exciton may happen between SWCNT and MoS_2NT, which could cause the enhancement of the absorption of MoS_2 in $SWCNT@BNNT@MoS_2NT$.

The PL quenching in the $SWCNT@BNNT@MoS_2NT$ sample is significant compared with the PL of $BNNT@MoS_2NT$. The near-field coupling, for example interlayer charge and/or energy transfer, is the main reason for causing the PL quenching effect.[40] To analyze the interaction between the SWCNT and MoS_2, we plotted the PL spectrum of $SWCNT@BNNT@MoS_2NT$ in the Raman shift, enlarged PL peak for both samples, and performed X-ray photoelectron spectroscopy (XPS) measurements (Figure S3 and S4). In Figure S4a, there is a noticeable blue shift of the PL from $SWCNT@BNNT@MoS_2NT$ with respect to the PL from $BNNT@MoS_2NT$ which verifies the hole doping (p-dope) in MoS_2NTs of $SWCNT@BNNT@MoS_2NT$.[41, 42] The Raman spectrum of SWCNT in $SWCNT@BNNT@MoS_2NT$ heteronanotubes (Figure S4b black

line) presents the typical electron doping (n-dope) effect based on the downshift of the G and 2D peak position.[43, 44] Though the downshift of Raman peaks from the SWCNT might result from the strain in the nanotube. However, the C1s peak of SWCNT@BNNT@MoS$_2$NT heteronanotubes in Figure S4c presents 0.2 eV shifting to higher binding energy with respect to the C1s peak of pristine SWCNT film which adds additional proof of the n-dope of SWCNT in the heteronanotubes. Furthermore, the comparison of B 1s and N 1s between the XPS spectra of SWCNT@BNNT@MoS$_2$NT and BNNT in Figure S5 confirms the stable chemical status of BN layer in the heteronanotubes. Therefore, in SWCNT@BNNT@MoS$_2$NT heteronanotubes, the net electron transfers from MoS$_2$NT to SWCNT causing the n-dope of SWCNT, and which naturally implies hole accumulated in MoS$_2$NT resulting in the doping to the p-direction of MoS$_2$NT. Hence, charge transfer occurs between SWCNT and MoS$_2$NT in the SWCNT@BNNT@MoS$_2$NT heteronanotube. Although electrons may transfer to SWCNT referring to the interpretation from our experimental data, the interlayer charge transfer process alone cannot be responsible for the massive PL quenching. Instead, interlayer energy transfer provides a highly efficient relaxation pathway[40] for excitons in SWCNT@BNNT@MoS$_2$NT heteronanotubes. Thus, in SWCNT@BNNT@MoS$_2$NT heteronanotubes, charge transfer probably happens in the ground state while energy transfer obviously happens after the photo-excitation which together result in the PL quenching effect. This conclusion is still a preliminary hypothesis, however, more detailed investigations need to be applied to confirm it in the future.

Raman spectra of 2D monolayer MoS$_2$, BNNT@MoS$_2$NT, SWCNT@BNNT@MoS$_2$NT, and bulk MoS$_2$ are shown in Figure 2c. The in-plane E_{2g}^1 and out-of-plane A_{1g} Raman modes of MoS$_2$ were observed in our BNNT@MoS$_2$NT and SWCNT@BNNT@MoS$_2$NT samples. The frequencies of both modes in single-walled MoS$_2$NTs in heteronanotubes are almost same as the monolayer MoS$_2$ values. The frequency difference of two modes is about 21 cm^{-1} which is identical with the monolayer MoS$_2$ sample. From the previous study, the E_{2g}^1 vibration softens (red shifts), while the A_{1g} vibration stiffens (blue shifts) with increasing thickness of 2D MoS$_2$ films.[45] However, we did not observe any clear softening or stiffening of the Raman modes in single-walled MoS$_2$NTs compared with monolayer MoS$_2$ though the curvature and strain energy in nanotubes are different.

Band structure of single-walled MoS$_2$NTs. A monolayer MoS$_2$ is well known as a semiconductor with a direct bandgap at the K point in the Brillouin zone,[19] while MoS$_2$NTs have been predicted as a semiconductor with an indirect bandgap except zigzag types.[21] In the previous studies, the band edge is based on the effect of strain from the curvature, which induces an increase of the energy levels of valence band edge around Γ point that forms an indirect bandgap with the bottom of the conduction band originated from the monolayer 2D K point. For the zigzag MoS$_2$NTs, however, they have direct bandgap because the K and Γ points are folded at the same place in the one-dimensional Brillouin zone of a nanotube. Because this special folding is only possible for the zigzag nanotube, all chiral nanotubes are expected to behave as indirect semiconductors like armchair nanotubes.[22] Here we suspected that the effect of the strain would decrease as the diameter of a nanotube becomes larger. When the diameter of a nanotube reached a certain size, reduced strain would make the bandgap of a nanotube approach the direct bandgap as a monolayer MoS$_2$. Figure 3a, 3b and 3c present the electronic structure of three types of single-walled MoS$_2$NTs with chiral indices of (12,12), (24,24), and (36,36) that are calculated by a density functional theory.[46, 47] The energy is measured with respect to that of the valence band edge at the Γ point. When the diameter of MoS$_2$NT is small, for example (12,12) chirality (Figure 3a), single-walled MoS$_2$NT is an indirect bandgap semiconductor. The valence peak at near $k = 2\pi/3$, originated from the K point of the Brillouin zone, becomes higher when the diameter of the nanotube increases. In fact, our calculations show that as the diameter of nanotube increased to 4.2 nm (Figure 3b), single-walled MoS$_2$NT still has an indirect bandgap but with near degenerate direct and indirect bandgap values.[48] Further, for the chiral index of (36,36) with diameter about 6.3 nm, the band degeneracy happened and the nanotube becomes a direct bandgap as shown in Figure 3c. Figure 3d shows the bandgap of armchair MoS$_2$NTs as a function of diameter. The cross-over between an indirect bandgap and a direct bandgap occurs when the chiral index of the MoS$_2$NT is (30,30) with the diameter about 5.2 nm. Therefore, the simulation result indicates when the diameter of a MoS$_2$NT is larger than about 5.2 nm, the MoS$_2$NT is a semiconductor with a direct bandgap which corresponds with the PL signal observed in the BNNT@MoS$_2$NT heteronanotube in this paper.
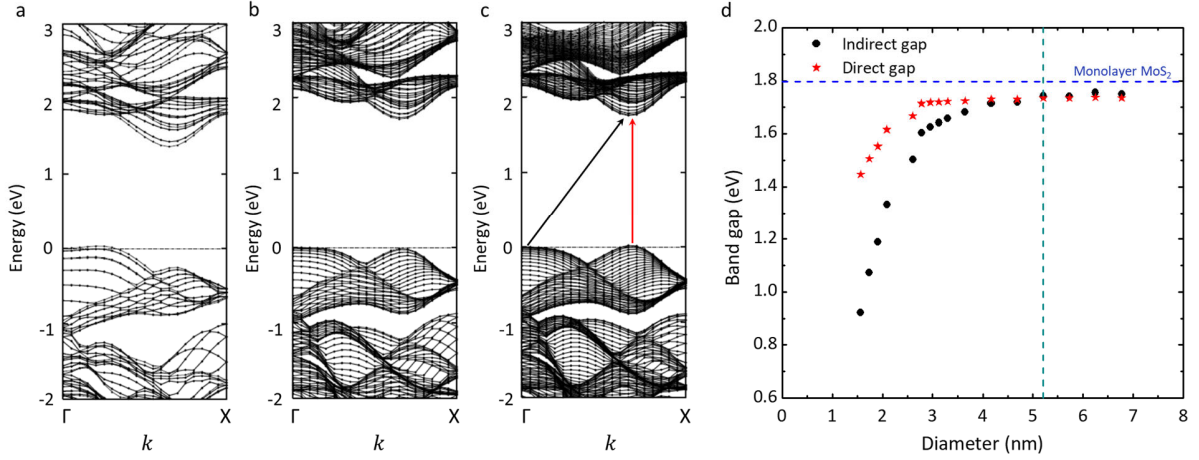
Figure 3. Calculated electronic structure of MoS$_2$NTs with different indices (a) (12,12) with diameter of 2.1 nm, (b) (24,24) with diameter of 4.2 nm, and (c) (36,36) with diameter of 6.3 nm. (d) The bandgap values of armchair MoS$_2$NTs as a function of diameter. The blue horizontal dot line indicates the value of band gap for monolayer MoS$_2$.

Structure of BNNT@MoS$_2$NT and BNNT@*multi*-MoS$_2$NT heteronanotubes. The heteronanotubes of BNNT@MoS$_2$NT were systematically characterized by optical measurements for example PL, Raman spectroscopy, and absorption. Here, multi-walled MoS$_2$ nanotubes coaxially grown on BNNTs (BNNT@*multi*-MoS$_2$NT) were synthesized by modifying the MoS$_2$ CVD parameters for studying the difference of the optical properties between BNNT@MoS$_2$NT and BNNT@*multi*-MoS$_2$NT nanotubes. The representative TEM images of BNNT@MoS$_2$NT and BNNT@*multi*-MoS$_2$NT nanotubes are shown in Figure S6. In Figure S6a, the MoS$_2$NTs coaxially grown on BNNTs are single-walled nanotubes, whereas the MoS$_2$ nanotubes in Figure S6b have two or three walls. Although there are some single-walled MoS$_2$NTs in the BNNT@*multi*-MoS$_2$NT, multi-walled MoS$_2$NTs are the majority. These two types of samples were used in the following optical characterizations.

The comparison of Raman, PL, and absorption spectra of BNNT@MoS$_2$NT and BNNT@*multi*-MoS$_2$NT heteronanotubes. Figure 4a shows representative Raman spectra of BNNT@ MoS$_2$NT and BNNT@*multi*-MoS$_2$NT samples with the excitation wavelength of 532 nm in air ambient environment. The E_{2g}^1 and A_{1g} modes were observed in both BNNT@ MoS$_2$NT and BNNT@*multi*-MoS$_2$NT samples. The in-plane E_{2g}^1 mode is associated with opposite vibration of

two S atoms with respect to the Mo atom, whereas the out-of-plane A_{1g} mode origins from the vibration of S atoms in opposite directions.[49, 50] For BNNT@MoS$_2$NT sample, the peak of the A_{1g} mode is at 405 cm^{-1} and the E_{2g}^1 mode locates at 384 cm^{-1}. Strikingly, we found the E_{2g}^1 vibration softened to ~380 cm^{-1} (red shifts), while the A_{1g} mode remained at the same position (~405 cm^{-1}) in the BNNT@*multi*-MoS$_2$NT sample. When the wall number increases, the interlayer van der Waals force in MoS$_2$ suppresses atom vibration, resulting in higher force constants.[51] However, the softening of E_{2g}^1 vibration and the negligible change of A_{1g} mode indicate the weaker interlayer interactions in MoS$_2$ cannot be only associated with the van der Waals interactions, instead there are addition interlayer interactions in the material.[45] The E_{2g}^1 and the A_{1g} vibrations in BNNT@*multi*-MoS$_2$NT both softened compared with these two modes in bulk MoS$_2$. The possible factors of causing softening of the two active Raman modes are the tensile strain in nanotubes which have a strong effect on the phonon dispersion[52] and the incommensurate stacking of layers in the multi-walled MoS$_2$NTs.[53]

Moreover, there are more Raman peaks in Figure 4c using the excitation wavelength of 632.8 nm which is in resonance with the direct band gap (~1.96 eV) of MoS$_2$ at the K point.[54] In the resonant Raman spectra, the most prominent mode around 460 cm^{-1} arises from a second-order process of involving the longitudinal acoustic phonons at M point (LA(M)).[50] On the spectrum of BNNT@*multi*-MoS$_2$NT, the peaks around 178, 453, and 637 cm^{-1} were observed as well the E_{2g}^1 (380 cm^{-1}) and A_{1g} (405 cm^{-1}) peaks. The peak at 453 cm^{-1} is assigned as the double frequency of the LA(M) mode. Moreover the peaks centered at 178 and 637 cm^{-1} are assigned to $A_{1g} - $ LA and $A_{1g} + $ LA Raman modes, respectively. The shoulder of A_{1g} peak in BNNT@*multi*-MoS$_2$NT evolves into an individual peak at 421 cm^{-1} in BNNT@MoS$_2$NT. This peak has been interpreted through a Raman-inactive mode (B$_{1u}$) due to a two-phonon scattering process involving a longitudinal quasi-acoustic phonon and a transverse optical phonon.[50] Moreover, on the Raman spectrum of BNNT@MoS$_2$NT, a blue-shift of the E_{2g}^1 (385 cm^{-1}) and A_{1g} (407 cm^{-1}) peaks was both observed respect to the two modes in BNNT@*multi*-MoS$_2$NT. Interestingly, the intensity of $A_{1g} - $ LA and $A_{1g} + $ LA vibration modes become much weaker in BNNT@MoS$_2$NT. Besides, the resonant Raman spectrum of BNNT@MoS$_2$NT is gradually lift-up of background towards high frequencies which is attributed to the tail of the PL signal in single-walled MoS$_2$NTs. These significant differences of the Raman features between BNNT@MoS$_2$NT and BNNT@*multi*-

MoS$_2$NT imply that Raman spectroscopy could serve as a reliable tool for distinguishing single-walled and multi-walled MoS$_2$NTs.

The absorption spectrum of BNNT@MoS$_2$NT was found to be mostly unaltered compared with the absorption spectrum of BNNT@*multi*-MoS$_2$NT, except for a slight blueshift of the resonances (Figure 4b). The PL peak (A) from BNNT@MoS$_2$NT at 1.85 eV almost matches the lower absorption resonance in its position (Figure 4d). Furthermore, the significantly quenched PL signal from BNNT@*multi*-MoS$_2$NT indicates that the multi-walled MoS$_2$ nanotube have an indirect bandgap which is similar to multilayer 2D MoS$_2$.[55] It is worth to mention here that a bright direct exciton emission at 10 K from MoS$_2$ nanotubes with the diameters of around 400 nm which possesses an indirect bandgap has been reported lately.[56] The temperature dependent photoluminescence studies of multi-walled MoS$_2$NT requires additional research to discover promising phenomenon.
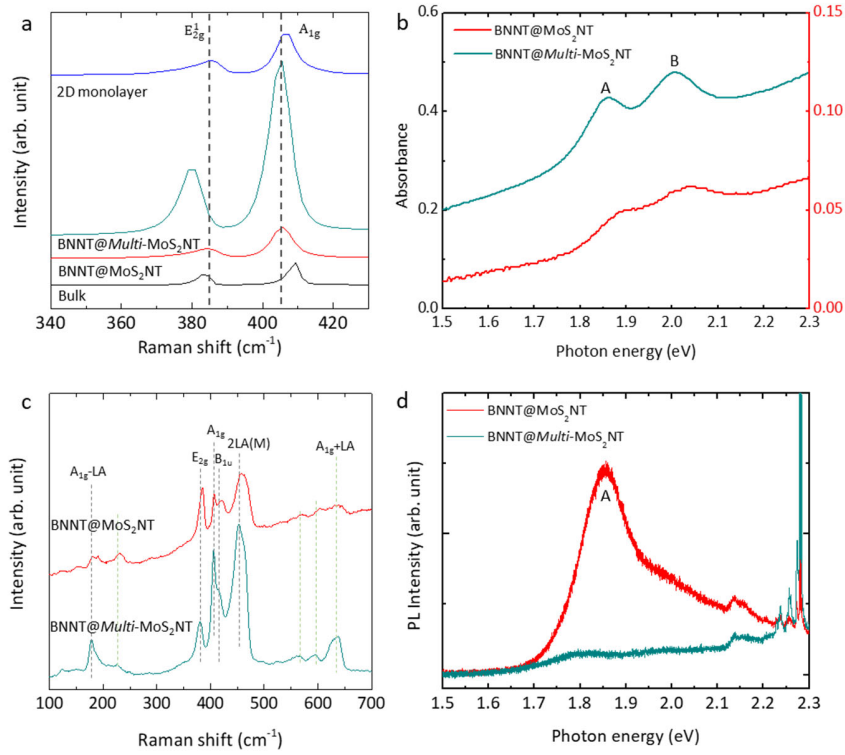
Figure 4. (a) Raman spectra of 2D monolayer MoS_2, BNNT@*multi*-MoS_2NT, BNNT@MoS_2NT, and the bulk MoS_2 with the excitation wavelength of 532 nm. (b) Representative absorption spectra of BNNT@MoS_2NT and BNNT@*multi*-MoS_2NT heteronanotubes. (c) Resonant Raman spectra of BNNT@MoS_2NT and BNNT@*multi*-MoS_2NT heteronanotubes using 632.8 nm laser. (d) PL spectra of BNNT@MoS_2NT and BNNT@*multi*-MoS_2NT heteronanotubes with 532 nm excited laser.

Conclusions

In conclusion, heteronanotubes of single- and multi-walled MoS_2 nanotubes coaxially grown on BNNTs were synthesized in this work. We observed the PL signal from single-walled MoS_2 nanotubes grown on BNNTs, and this result corresponded with our DFT results that large-diameter single-walled MoS_2NTs have a direct bandgap at K point that is originated from the 2D K point. Meanwhile, the PL signal of single-walled MoS_2NTs in SWCNT@BNNT@MoS_2NT heteronanotubes is noticeably quenched. The charge and energy transfer between SWCNTs and single-walled MoS_2NTs in one-dimensional van der Waals heterostructures were examined by PL and Raman spectroscopy. The significant PL quenching in multi-walled MoS_2NTs verified their indirect bandgap structures. The different Raman features of single-walled and multi-walled MoS_2NTs under resonant and non-resonant conditions may provide a tool for distinguishing between single-walled and multi-walled MoS_2NTs. The BNNT based hetero structure may provide an efficient approach for investigating the optical properties of TMD nanotubes.

Methods

Synthesis of the BNNT Film. The SWCNT film used in this work as a template was synthesized by aerosol CVD and collected on a filter paper.[57] The diameter distribution of the SWCNTs produced by this method is in the range of 1.3–2.0 nm. The SWCNT film with filter paper was dry-transferred onto a ceramic washer (6 mm). After removing the filter paper, the SWCNT film was suspended on the ceramic washer. For the BNNT CVD, the BN precursor, 30 mg of borane-ammonia complex (97%, Sigma-Aldrich), was placed upstream in the quartz tube and heated to 70°C. A low-pressure CVD with 300 Pa was applied here for the reaction at 1075°C and Ar with 3% H_2 was the carrier gas for the BN precursor with a flow rate of 300 sccm. The representative CVD time here was 1 hour and the average coating ratio was around 55%. After the BNNT coating CVD procedure, samples were set in a pure O_2 atmosphere CVD system for thermal oxidizing the inner SWCNT film to obtain the pure BNNT film. The oxidation process was taken at 610°C at 85kPa with a flow rate of 45 sccm O_2 gas for 12 hours.

Growth of the BNNT@MoS$_2$NT film. The BNNT@MoS$_2$NT heteronanotube was synthesized by a low-pressure CVD system using sulfur (sublimated, 99.0%, Wako) and MoO_3 (99.9%, Sigma-Aldrich) powders as precursors. Sulfur(S) powder (5 g) was loaded in a quartz boat and placed out of the furnace at the upstream of the quartz tube chamber. The S quartz boat was heated up by a rubber heater to 138 °C. MoO_3 powder (35 mg) was placed upstream of the substrates and heated up to 530 °C. The BNNT film sample was set downstream of the MoO_3 powder and heated up to 530 °C for synthesizing single-walled MoS$_2$NTs and 750 °C for multi-walled MoS$_2$NTs. Ar gas with a flow rate of 50 sccm was introduced into the chamber as a carrier. The typical reaction time at aimed temperature was 10 min. The distance of the MoO_3 quartz boat and the substrate is an essential parameter for controlling the quality of MoS_2. The distance in this experiment was 10 cm. The diameter of the quartz tube chamber is 25 mm.

Optical characterizations and TEM characterizations. The Raman and PL spectra of the samples were obtained by a Raman spectrometer (inVia, Renishaw) with the excitation wavelengths of 532 nm and 632.8 nm. The absorption spectra were measured by a UV-Vis-NIR spectrophotometer (Shimadzu UV-3150). The photo-emission measurements were performed using XPS (PHI5000, Versa Probe) with monochromatic Al Kα radiation. The TEM images were obtained by a JEM-2010F microscope and a JEM-2800 microscope at an acceleration voltage of

200 kV or 100 kV. The high-resolution TEM images were taken by a JEM-ARM200F microscope with a thermal field-emission gun operating at 120 kV.

DFT Calculation. The Simulation Tool for Atom Technology (STATE)[58] package was used for investigating the geometric and electronic structures. General gradient approximation by Perdew-Burke-Ernzerhof functional[59, 60] was applied to describe exchange correlation potential energy between electrons. Ultrasoft pseudopotentials were used for the pseudopotential between electrons and ions.[61] Cutoff energies of plane-wave to expand the valence wavefunction and deficit charge density were 340 and 3061 eV (25 and 225 Ry), respectively. Atomic structure was optimized until forces acting on each atom are less than 0.684 eV/nm (1.33×10^{-3} Hartree/au). A lattice parameter along tube direction was fixed to 0.315 nm, which corresponds with the experimental value of bulk MoS_2.[62] The Brillouin zone integration was carried out under six k points along the tube direction.

Supporting Information

Optical characterizations of BNNTs film, TEM images of SWCNT@BNNT@MoS$_2$NT, BNNT@MoS$_2$NT and BNNT@*multi*-MoS$_2$NT heterostructures, absorption spectra of SWCNT, SWCNT@BNNT@MoS$_2$NT and BNNT@MoS$_2$NT films, and XPS characterization results.

Author Contributions

M.L. and S.M. conceived the research; M.L., K.H., S.S., A.A., and R.X. performed research; M.L. synthesized different 1D heteronanotubes and performed Raman, absorption, and PL characterizations; M.L. and R.X. took HR-TEM images; K.H. performed DFT calculation; R.X. made atomic models; S.S. performed XPS characterization; M.L. and S.M. analyzed the data; M.L. wrote the manuscript; all co-authors participated in the discussion and commented on the manuscript.

Acknowledgements

References

(1) Geim, A. K.; Grigorieva, I. V. van der Waals Heterostructures. *Nature* **2013,** 499, 419-425.

(2) Wang, Q. H.; Kalantar-Zadeh, K.; Kis, A.; Coleman, J. N.; Strano, M. S. Electronics and Optoelectronics of Two-Dimensional Transition Metal Dichalcogenides. *Nat. Nanotechnol.* **2012,** 7, 699-712.

(3) Chhowalla, M.; Shin, H. S.; Eda, G.; Li, L.-J.; Loh, K. P.; Zhang, H. The Chemistry of Two-Dimensional Layered Transition Metal Dichalcogenide Nanosheets. *Nat. Chem.* **2013,** 5, 263-275.

(4) Fiori, G.; Bonaccorso, F.; Iannaccone, G.; Palacios, T.; Neumaier, D.; Seabaugh, A.; Banerjee, S. K.; Colombo, L. Electronics Based on Two-Dimensional Materials. *Nat. Nanotechnol.* **2014,** 9, 768-779.

(5) Jariwala, D.; Sangwan, V. K.; Lauhon, L. J.; Marks, T. J.; Hersam, M. C. Emerging Device Applications for Semiconducting Two-Dimensional Transition Metal Dichalcogenides. *ACS nano* **2014,** 8, 1102-1120.

(6) Zhang, H. Ultrathin Two-Dimensional Nanomaterials. *ACS nano* **2015,** 9, 9451-9469.

(7) Liu, Y.; Weiss, N. O.; Duan, X.; Cheng, H.-C.; Huang, Y.; Duan, X. van der Waals Heterostructures and Devices. *Nat. Rev. Mater.* **2016,** 1, 1-17.

(8) Cui, X.; Lee, G.-H.; Kim, Y. D.; Arefe, G.; Huang, P. Y.; Lee, C.-H.; Chenet, D. A.; Zhang, X.; Wang, L.; Ye, F.; Pizzocchero, F.; Jessen, B. S.; Watanabe, K.; Taniguchi, T.; Muller, D. A.; Low, T.; Kim, P.; Hone, J. Multi-Terminal Transport Measurements of MoS$_2$ Using a van der Waals Heterostructure Device Platform. *Nat. Nanotechnol.* **2015,** 10, 534-540.

(9) Tenne, R. Advances in the Synthesis of Inorganic Nanotubes and Fullerene-Like Nanoparticles. *Angew. Chem. Int. Ed.* **2003,** 42, 5124-5132.

(10) Xiang, R.; Inoue, T.; Zheng, Y.; Kumamoto, A.; Qian, Y.; Sato, Y.; Liu, M.; Tang, D.; Gokhale, D.; Guo, J.; Hisama, K.; Yotsumoto, S.; Ogamoto, T.; Arai, H.; Kobayashi, Y.; Zhang, H.; Hou, B.; Anisimov, A.; Maruyama, M.; Miyata, Y; et al. One-Dimensional van der Waals Heterostructures. *Science* **2020,** 367, 537-542.

(11) Feldman, Y.; Wasserman, E.; Srolovitz, D.; Tenne, R. High-Rate, Gas-Phase Growth of MoS$_2$ Nested Inorganic Fullerenes and Nanotubes. *Science* **1995,** 267, 222-225.

(12) Seifert, G.; Köhler, T.; Tenne, R. Stability of Metal Chalcogenide Nanotubes. *J. Phys. Chem. B* **2002,** 106, 2497-2501.

(13) Remskar, M.; Skraba, Z.; Cléton, F.; Sanjinés, R.; Lévy, F. MoS$_2$ as Microtubes. *Appl. Phys. Lett.* **1996,** 69, 351-353.

(14) Remškar, M. Inorganic Nanotubes. *Adv. Mater.* **2004,** 16, 1497-1504.

(15) Remskar, M.; Mrzel, A.; Skraba, Z.; Jesih, A.; Ceh, M.; Demšar, J.; Stadelmann, P.; Lévy, F.; Mihailovic, D. Self-Assembly of Subnanometer-Diameter Single-Wall MoS$_2$ Nanotubes. *Science* **2001,** 292, 479-481.

(16) Roxlo, C.; Chianelli, R.; Deckman, H.; Ruppert, A.; Wong, P. Bulk and Surface Optical Absorption in Molybdenum Disulfide. *J. Vac. Sci. Technol. A* **1987,** 5, 555-557.

(17) Li, T.; Galli, G. Electronic Properties of MoS$_2$ Nanoparticles. *J. Phys. Chem. C* **2007,** 111, 16192-16196.

(18) Mak, K. F.; Lee, C.; Hone, J.; Shan, J.; Heinz, T. F. Atomically Thin MoS$_2$: A New Direct-Gap Semiconductor. *Phys. Rev. Lett.* **2010,** 105, 136805.

(19) Splendiani, A.; Sun, L.; Zhang, Y.; Li, T.; Kim, J.; Chim, C.-Y.; Galli, G.; Wang, F. Emerging Photoluminescence in Monolayer MoS$_2$. *Nano Lett.* **2010,** 10, 1271-1275.

(20) Eda, G.; Yamaguchi, H.; Voiry, D.; Fujita, T.; Chen, M.; Chhowalla, M. Photoluminescence from Chemically Exfoliated MoS$_2$. *Nano Lett.* **2011,** 11, 5111-5116.

(21) Seifert, G.; Terrones, H.; Terrones, M.; Jungnickel, G.; Frauenheim, T. Structure and Electronic Properties of MoS$_2$ Nanotubes. *Phys. Rev. Lett.* **2000,** 85, 146.

(22) Zhang, D.-B.; Dumitrică, T.; Seifert, G. Helical Nanotube Structures of MoS$_2$ with Intrinsic Twisting: An Objective Molecular Dynamics Study. *Phys. Rev. Lett.* **2010,** 104, 065502.

(23) Zibouche, N.; Kuc, A.; Heine, T. From Layers to Nanotubes: Transition Metal Disulfides TMS$_2$. *Eur. Phys. J. B* **2012,** 85, 49.

(24) Milošević, I.; Nikolić, B.; Dobardžić, E.; Damnjanović, M.; Popov, I.; Seifert, G. Electronic Properties and Optical Spectra of MoS_2 and WS_2 Nanotubes. *Phys. Rev. B* **2007,** 76, 233414.

(25) Zhu, Y. Q.; Hsu, W. K.; Kroto, H. W.; Walton, D. R. M. Carbon Nanotube Template Promoted Growth of NbS_2 Nanotubes/Nanorods. *Chem. Commun.* **2001**, 2184-2185.

(26) Whitby, R. L.; Hsu, W. K.; Fearon, P. K.; Billingham, N. C.; Maurin, I.; Kroto, H. W.; Walton, D. R.; Boothroyd, C. B.; Firth, S.; Clark, R. J.; Collison, D. Multiwalled Carbon Nanotubes Coated with Tungsten Disulfide. *Chem. Mater.* **2002,** 14, 2209-2217.

(27) Meyer, R. R.; Sloan, J.; Dunin-Borkowski, R. E.; Kirkland, A. I.; Novotny, M. C.; Bailey, S. R.; Hutchison, J. L.; Green, M. L. Discrete Atom Imaging of One-Dimensional Crystals Formed within Single-Walled Carbon Nanotubes. *Science* **2000,** 289, 1324-1326.

(28) Philp, E.; Sloan, J.; Kirkland, A. I.; Meyer, R. R.; Friedrichs, S.; Hutchison, J. L.; Green, M. L. An Encapsulated Helical One-Dimensional Cobalt Iodide Nanostructure. *Nat. Mater.* **2003,** 2, 788-791.

(29) Koroteev, V.; Bulusheva, L.; Asanov, I.; Shlyakhova, E.; Vyalikh, D.; Okotrub, A. Charge Transfer in the MoS_2/Carbon Nanotube Composite. *J. Phys. Chem. C* **2011,** 115, 21199-21204.

(30) Burdanova, M. G.; Kashtiban, R. J.; Zheng, Y.; Xiang, R.; Chiashi, S.; Woolley, J. M.; Staniforth, M.; Sakamoto-Rablah, E.; Xie, X.; Broome, M.; Sloan, J.; Anisimov, A.; Kauppinen, E. I.; Maruyama, S.; Lloyd-Hughes, J. Ultrafast Optoelectronic Processes in 1D Radial van der Waals Heterostructures: Carbon, Boron Nitride, and MoS_2 Nanotubes with Coexisting Excitons and Highly Mobile Charges. *Nano Lett.* **2020,** 20, 3560-3567.

(31) Wang, Y.; Ma, Z.; Chen, Y.; Zou, M.; Yousaf, M.; Yang, Y.; Yang, L.; Cao, A.; Han, R. P. Controlled Synthesis of Core–Shell Carbon@MoS_2 Nanotube Sponges as High-Performance Battery Electrodes. *Adv. Mater.* **2016,** 28, 10175-10181.

(32) Dresselhaus, M. S.; Dresselhaus, G.; Saito, R.; Jorio, A. Raman Spectroscopy of Carbon Nanotubes. *Phys. Rep.* **2005,** 409, 47-99.

(33) Lefebvre, J.; Fraser, J.; Finnie, P.; Homma, Y. Photoluminescence from an Individual Single-Walled Carbon Nanotube. *Phys. Rev. B* **2004,** 69, 075403.

(34) Golberg, D.; Bando, Y.; Tang, C.; Zhi, C. Boron Nitride Nanotubes. *Adv. Mater.* **2007,** 19, 2413-2432.

(35) Lee, C. H.; Xie, M.; Kayastha, V.; Wang, J.; Yap, Y. K. Patterned Growth of Boron Nitride Nanotubes by Catalytic Chemical Vapor Deposition. *Chem. Mater.* **2010,** 22, 1782-1787.

(36) Virsek, M.; Krause, M.; Kolitsch, A.; Remškar, M. Raman Characterization of MoS_2 Microtube. *Phys. Status Solidi (b)* **2009,** 246, 2782-2785.

(37) Coehoorn, R.; Haas, C.; De Groot, R. Electronic Structure of $MoSe_2$, MoS_2, and WSe_2. II. The Nature of the Optical Band Gaps. *Phys. Rev. B* **1987,** 35, 6203.

(38) Kam, K.; Parkinson, B. Detailed Photocurrent Spectroscopy of the Semiconducting Group VIB Transition Metal Dichalcogenides. *J. Phys. Chem.* **1982,** 86, 463-467.

(39) Evans, B.; Young, P. Optical Absorption and Dispersion in Molybdenum Disulphide. *Proc. Math. and Phys. Eng. Sci.* **1965,** 284, 402-422.

(40) Froehlicher, G.; Lorchat, E.; Berciaud, S. Charge *versus* Energy Transfer in Atomically Thin Graphene-Transition Metal Dichalcogenide van der Waals Heterostructures. *Phys. Rev. X* **2018,** 8, 011007.

(41) Mak, K. F.; He, K.; Lee, C.; Lee, G. H.; Hone, J.; Heinz, T. F.; Shan, J. Tightly Bound Trions in Monolayer MoS_2. *Nat. Mater.* **2013,** 12, 207-211.

(42) Mouri, S.; Miyauchi, Y.; Matsuda, K. Tunable Photoluminescence of Monolayer MoS_2 *via* Chemical Doping. *Nano Lett.* **2013,** 13, 5944-5948.

(43) Rao, A. M.; Eklund, P.; Bandow, S.; Thess, A.; Smalley, R. E. Evidence for Charge Transfer in Doped Carbon Nanotube Bundles from Raman Scattering. *Nature* **1997,** 388, 257-259.

(44) Corio, P.; Santos, P.; Brar, V.; Samsonidze, G. G.; Chou, S.; Dresselhaus, M. Potential Dependent Surface Raman Spectroscopy of Single Wall Carbon Nanotube Films on Platinum Electrodes. *Chem. Phys. Lett.* **2003,** 370, 675-682.

(45) Lee, C.; Yan, H.; Brus, L. E.; Heinz, T. F.; Hone, J.; Ryu, S. Anomalous Lattice Vibrations of Single- and Few-layer MoS_2. *ACS nano* **2010,** 4, 2695-2700.

(46) Kohn, W.; Sham, L. J. Self-Consistent Equations Including Exchange and Correlation Effects. *Phys. Rev.* **1965,** 140, A1133.

(47) Hohenberg, P.; Kohn, W. Inhomogeneous Electron Gas. *Phys. Rev.* **1964,** 136, B864.

(48) Tongay, S.; Zhou, J.; Ataca, C.; Lo, K.; Matthews, T. S.; Li, J.; Grossman, J. C.; Wu, J. Thermally Driven Crossover from Indirect toward Direct Bandgap in 2D Semiconductors: $MoSe_2$ *versus* MoS_2. *Nano Lett.* **2012,** 12, 5576-5580.

(49) Bertrand, P. Surface-Phonon Dispersion of MoS_2. *Phys. Rev. B* **1991,** 44, 5745.

(50) Li, H.; Zhang, Q.; Yap, C. C. R.; Tay, B. K.; Edwin, T. H. T.; Olivier, A.; Baillargeat, D. From Bulk to Monolayer MoS_2: Evolution of Raman Scattering. *Adv. Funct. Mater.* **2012,** 22, 1385-1390.

(51) Bagnall, A.; Liang, W.; Marseglia, E.; Welber, B. Raman Studies of MoS_2 at High Pressure. *Phys. B+ C* **1980,** 99, 343-346.

(52) Ghorbani-Asl, M.; Zibouche, N.; Wahiduzzaman, M.; Oliveira, A. F.; Kuc, A.; Heine, T. Electromechanics in MoS_2 and WS_2: Nanotubes *vs*. Monolayers. *Sci. Rep.* **2013,** 3, 2961.

(53) Zhou, X.; Jin, K.; Cong, X.; Tan, Q.; Li, J.; Liu, D.; Luo, J. Interlayer Interaction on Twisted Tnterface in Incommensurate Stacking MoS_2: A Raman Spectroscopy Study. *J. Colloid Interface Sci.* **2019,** 538, 159-164.

(54) Windom, B. C.; Sawyer, W.; Hahn, D. W. A Raman Spectroscopic Study of MoS_2 and MoO_3: Applications to Tribological Systems. *Tribol. Lett.* **2011,** 42, 301-310.

(55) Yun, W. S.; Han, S. W.; Hong, S. C.; Kim, I. G.; Lee, J. D. Thickness and Strain Effects on Electronic Structures of Transition Metal Dichalcogenides: $2H-MX_2$ Semiconductors (M = Mo, W; X = S, Se, Te). *Phys. Rev. B* **2012,** 85, 033305.

(56) Shubina, T. V.; Remškar, M.; Davydov, V. Y.; Belyaev, K. G.; Toropov, A. A.; Gil, B. Excitonic Emission in van der Waals Nanotubes of Transition Metal Dichalcogenides. *Ann. Phys.* **2019,** 531, 1800415.

(57) Nasibulin, A. G.; Kaskela, A.; Mustonen, K.; Anisimov, A. S.; Ruiz, V.; Kivisto, S.; Rackauskas, S.; Timmermans, M. Y.; Pudas, M.; Aitchison, B.; Kauppinen, M.; Brown, D. P.; Okhotnikov, O. G.; Kauppinen, E. I. Multifunctional Free-Standing Single-Walled Carbon Nanotube Films. *ACS nano* **2011,** 5, 3214-3221.

(58) Morikawa, Y.; Iwata, K.; Terakura, K. Theoretical Study of Hydrogenation Process of Formate on Clean and Zn Deposited Cu (1 1 1) Surfaces. *Appl. Surf. Sci.* **2001,** 169, 11-15.

(59) Perdew, J. P.; Burke, K.; Ernzerhof, M. Generalized Gradient Approximation Made Simple. *Phys. Rev. Lett.* **1996,** 77, 3865.

(60) Perdew, J. P.; Burke, K.; Ernzerhof, M. Generalized Gradient Approximation Made Simple [Phys. Rev. Lett. 77, 3865 (1996)]. *Phys. Rev. Lett.* **1997,** 78, 1396-1396.

(61) Vanderbilt, D. Soft Self-Consistent Pseudopotentials in a Generalized Eigenvalue Formalism. *Phys. Rev. B* **1990,** 41, 7892.

(62) Wakabayashi, N.; Smith, H.; Nicklow, R. Lattice Dynamics of Hexagonal MoS_2 Studied by Neutron Scattering. *Phys. Rev. B* **1975,** 12, 659.

For Table of Contents Only
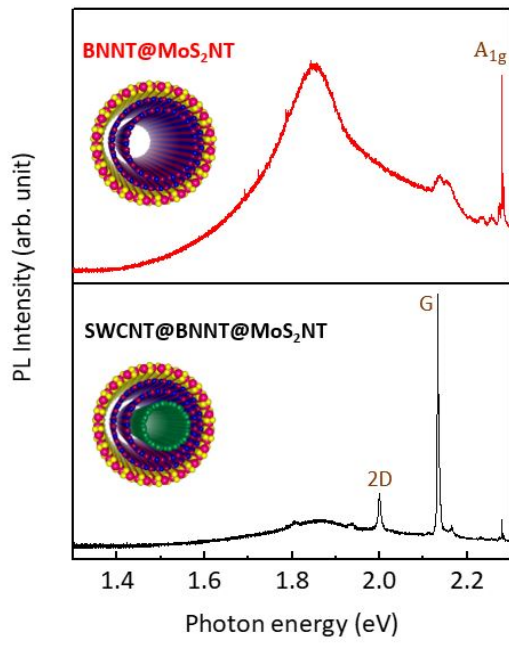
Supplementary information for:

Photoluminescence from Single-Walled MoS₂ Nanotubes Coaxially Grown on Boron Nitride Nanotubes

Ming Liu[1], Kaoru Hisama[1], Yongjia Zheng[1], Mina Maruyama[2], Seungju Seo[1], Anton Anisimov[3], Taiki Inoue[1,4], Esko I. Kauppinen[5], Susumu Okada[2], Shohei Chiashi[1], Rong Xiang[1], and Shigeo Maruyama[1]*

[1] *Department of Mechanical Engineering, The University of Tokyo, Tokyo 113-8656, Japan*

[2] *Graduate School of Pure and Applied Sciences, University of Tsukuba, Tsukuba 305-8571, Japan*

[3] *Canatu Ltd., Helsinki FI‑00390, Finland*

[4] *Department of Applied Physics, Graduate School of Engineering, Osaka University, Osaka 565-0871, Japan*

[5] *Department of Applied Physics, Aalto University School of Science, Espoo 15100, FI-00076 Aalto, Finland*

Figure S1. Representative (a) UV-Vis-NIR absorption spectra of free-standing SWCNT, SWCNT@BNNT, and BNNT films on ceramic washers. For the absorbance, $A = -\log_{10}(T/T_0)$ (b) Raman spectrum and (c) FT-IR spectrum of the free-standing BNNT film on a ceramic washer.
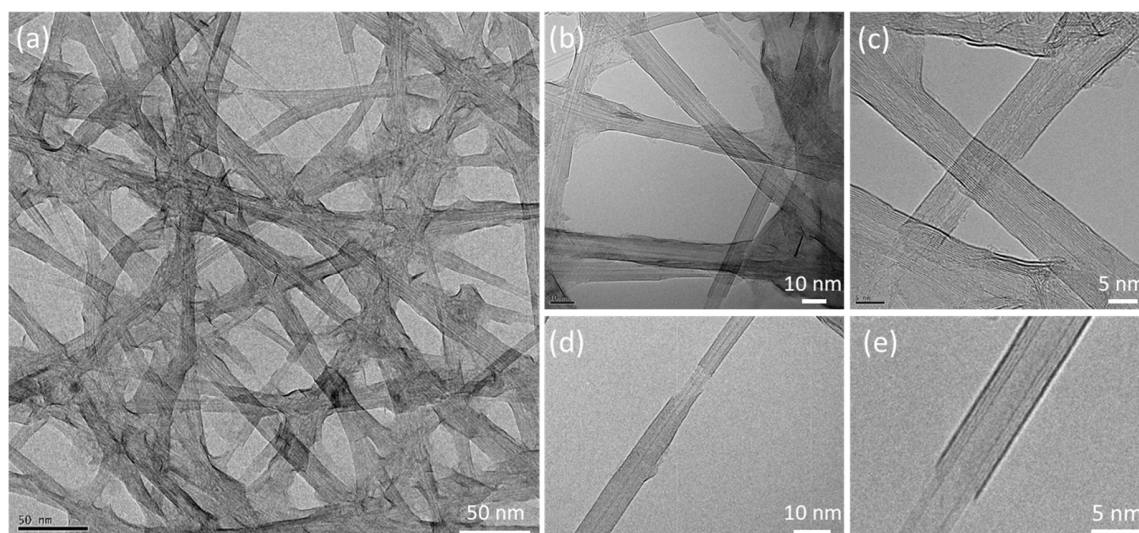

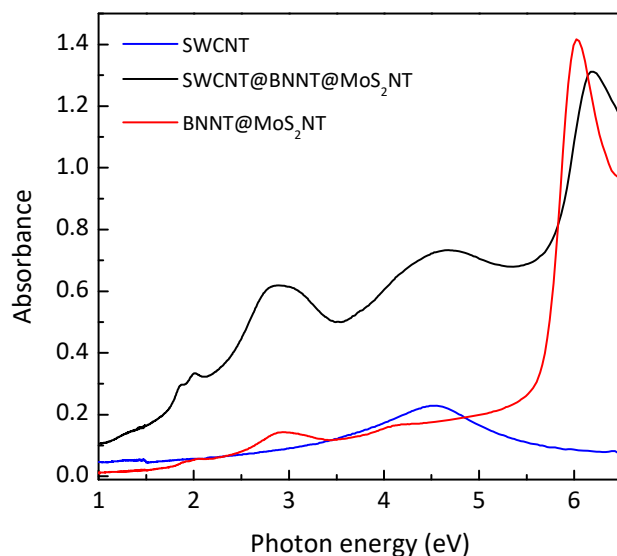Figure S2. (a) Low magnification and (b-e) high resolution TEM image of the SWCNT@BNNT@MoS$_2$NT heteronanotube.

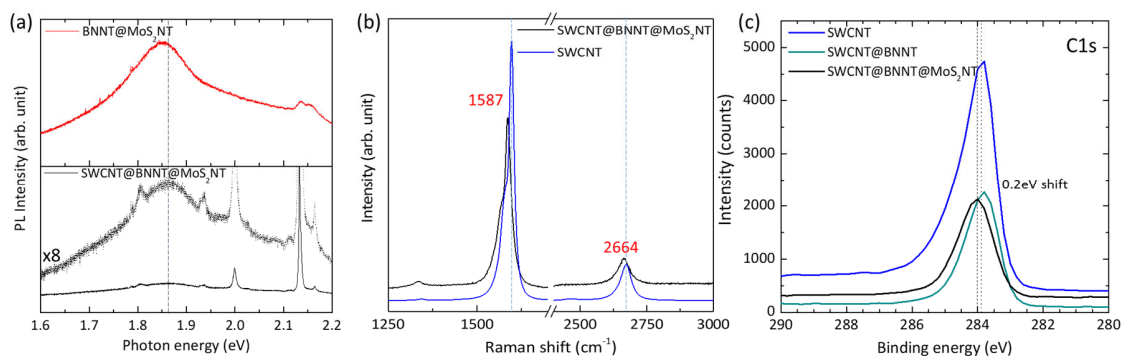Figure S3 (a) Absorption spectra of free-standing SWCNT, SWCNT@BNNT@MoS$_2$NT, and BNNT@MoS$_2$NT films.

Figure S4. (a) PL spectra of BNNT@MoS$_2$NT and SWCNT@BNNT@MoS$_2$NT heteronanotubes within 1.6-2.2 eV. (b) Raman spectrum of SWCNT@BNNT@MoS$_2$NT heteronanotubes and the pristine SWCNT film. (c) Representative XPS spectra of the pristine SWCNT film, SWCNT@BNNT film, and SWCNT@BNNT@MoS$_2$NT film.
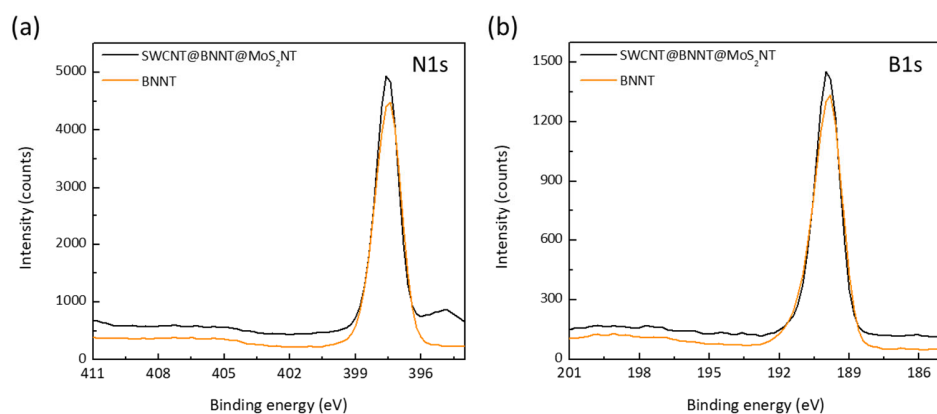
Figure S5. (a) N 1s and (B) B 1s XPS spectra shown, respectively, of a SWCNT@BNNT@MoS$_2$NT film and a BNNT film.
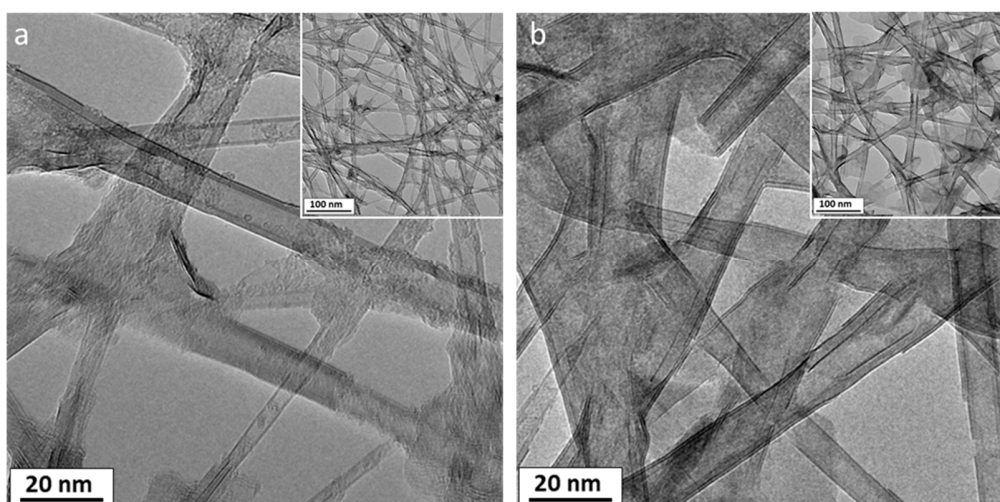

Figure S6. Representative TEM images of (a) BNNT@MoS$_2$NT and (b) BNNT@*multi*-MoS$_2$NT heteronanotubes. Insets are the low-magnification TEM images of two samples.
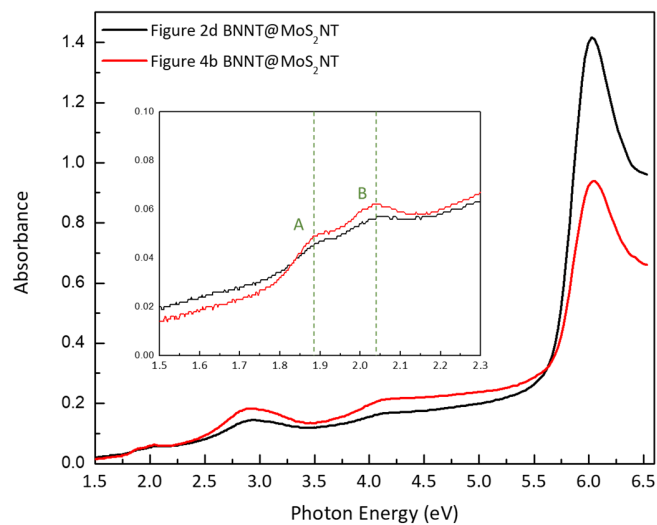
Figure S7. The absorption spectra of BNNT@MoS$_2$NT samples used in Figure 2d and Figure 4b.

In Figure 2d and Figure 4b, we have two different BNNT@MoS$_2$NT samples involved in total in our discussions. We used the same synthesis parameters and obtained two batches of samples, the BN amount in the two bathes is a bit different. Thus, to provide a fair comparison, we included four samples in the discussion, SWCNT@BNNT@MoS$_2$NT, BNNT@MoS$_2$NT in Figure2d, BNNT@MoS$_2$NT in Figure 4b, and BNNT@*multi*-MoS$_2$NT.